AGU PUBLICATIONS

JGR

Journal of Geophysical Research: Space Physics

RESEARCH ARTICLE
10.1002/2016JA023610

Key Points:
- Enhanced magnetospheric Pc5 ULF waves driven by magnetopause disturbances during northward IMF
- Waves driven by Kelvin-Helmholtz flow vortices
- Waves driven by foreshock perturbations resulting from IMF discontinuities

Correspondence to:
C.-P. Wang,
cat@atmos.ucla.edu

Citation:
Wang, C.-P., et al. (2017), A multispacecraft event study of Pc5 ultralow-frequency waves in the magnetosphere and their external drivers, *J. Geophys. Res. Space Physics*, *122*, doi:10.1002/2016JA023610.

Received 20 OCT 2016
Accepted 15 APR 2017
Accepted article online 24 APR 2017

A multispacecraft event study of Pc5 ultralow-frequency waves in the magnetosphere and their external drivers

Chih-Ping Wang[1], Richard Thorne[1], Terry Z. Liu[2], Michael D. Hartinger[3], Tsugunobu Nagai[4], Vassilis Angelopoulos[2], John R. Wygant[5], Aaron Breneman[5], Craig Kletzing[6], Geoffrey D. Reeves[7,8], Seth G. Claudepierre[9], and Harlan E. Spence[10]

[1]Department of Atmospheric and Oceanic Sciences, University of California, Los Angeles, California, USA, [2]Department of Earth, Planetary, and Space Sciences, University of California, Los Angeles, California, USA, [3]Department of Electrical and Computer Engineering, Virginia Tech, Blacksburg, Virginia, USA, [4]Department of Earth and Planetary Sciences, Tokyo Institute of Technology, Tokyo, Japan, [5]School of Physics and Astronomy, University of Minnesota, Minneapolis, Minnesota, USA, [6]Department of Physics and Astronomy, University of Iowa, Iowa City, Iowa, USA, [7]Space Science and Applications Group, Los Alamos National Laboratory, Los Alamos, New Mexico, USA, [8]New Mexico Consortium, Los Alamos, New Mexico, USA, [9]Space Sciences Department, Aerospace Corporation, El Segundo, California, USA, [10]Institute for the Study of Earth, Oceans, and Space, University of New Hampshire, Durham, New Hampshire, USA

Abstract We investigate a quiet time event of magnetospheric Pc5 ultralow-frequency (ULF) waves and their likely external drivers using multiple spacecraft observations. Enhancements of electric and magnetic field perturbations in two narrow frequency bands, 1.5–2 mHz and 3.5–4 mHz, were observed over a large radial distance range from $r \sim 5$ to 11 R_E. During the first half of this event, perturbations were mainly observed in the transverse components and only in the 3.5–4 mHz band. In comparison, enhancements were stronger during the second half in both transverse and compressional components and in both frequency bands. No indication of field line resonances was found for these magnetic field perturbations. Perturbations in these two bands were also observed in the magnetosheath, but not in the solar wind dynamic pressure perturbations. For the first interval, good correlations between the flow perturbations in the magnetosphere and magnetosheath and an indirect signature for Kelvin-Helmholtz (K-H) vortices suggest K-H surface waves as the driver. For the second interval, good correlations are found between the magnetosheath dynamic pressure perturbations, magnetopause deformation, and magnetospheric waves, all in good correspondence to interplanetary magnetic field (IMF) discontinuities. The characteristics of these perturbations can be explained by being driven by foreshock perturbations resulting from these IMF discontinuities. This event shows that even during quiet periods, K-H-unstable magnetopause and ion foreshock perturbations can combine to create a highly dynamic magnetospheric ULF wave environment.

1. Introduction

Ultralow-frequency (ULF) waves (~1 to 5000 mHz) in electric and magnetic fields are important to the dynamics of ring current particles and relativistic electrons by affecting their three adiabatic invariants [e.g., *Elkington et al*., 2003]. Studies have shown that there is a good correlation between relativistic electron enhancements and magnetospheric ULF wave power [*Rostoker et al*., 1998]. Storms with a long duration of elevated ULF wave activity in the inner magnetosphere are more likely to produce relativistic electrons than those without [*O'Brien et al*., 2001; *Reeves et al*., 2003]. It is thus important to understand the processes driving magnetospheric ULF waves. ULF waves in the near-Earth magnetosphere can be driven internally by nightside disturbances, such as substorms, or instabilities associated with cyclotron resonances or drift-bounce resonances [*McPherron*, 2005], or externally by magnetopause disturbances [e.g., *Hwang*, 2015]. ULF waves driven by magnetopause disturbances should play an important role during quiet times when the ULF waves driven by nightside disturbances and instabilities subside.

Magnetopause disturbances can be caused by mainly four different processes [*Hwang and Sibeck*, 2016]: (1) The initial disturbances can be embedded within the solar wind, such as solar wind dynamic pressure perturbations. (2) They can be created near the bow shock, such as density variations associated with foreshock perturbations. (3) They can be created within the magnetosheath by instabilities, such as variations associated with the mirror, cyclotron, and firehose instability. (4) They can be generated right at the magnetopause, such as flow perturbations associated with surface/Kelvin-Helmholtz (K-H) waves. There have been

many observational studies showing that magnetospheric ULF waves can be driven by solar wind dynamic pressure perturbations [e.g., *Korotova and Sibeck*, 1995; *Kepko and Spence*, 2003; *Viall et al*., 2009]. Even when the solar wind dynamic pressure is steady, observations and simulations have shown that foreshock perturbations, such as hot flow anomalies [e.g., *Thomsen et al*., 1986; *Zhang et al.*, 2010] and foreshock bubbles [e.g., *Omidi et al*., 2010; *Turner et al*., 2013], can create magnetosheath dynamic pressure perturbations and drive ULF waves in the magnetosphere [*Hartinger et al*., 2013; *Archer et al*., 2013]. Magnetosheath pressure anisotropy can lead to mirror [e.g., *Hasegawa*, 1971] or cyclotron instabilities [e.g., *Seough and Yoon*, 2012] if perpendicular pressure is larger, or to firehose instability if parallel pressure is larger [e.g., *Erickson et al*., 2002]. Magnetosheath mirror mode waves have been observed to cause magnetopause undulations [e.g., *Nowada et al*., 2009]. Using multiple spacecraft observations with one spacecraft near the magnetopause, *Takahashi et al.* [1991], *Rae et al.* [2005], and *Agapitov et al.* [2009] have shown ULF waves in the inner magnetosphere being driven by surface/K-H waves [*Chandrasekhar*, 1961].

Our current understanding of magnetospheric ULF waves driven by surface/K-H waves or foreshock perturbations remains very limited since only a few observational studies have been conducted (see references listed above). In this paper we present a quiet time event of Pc5 (1.66–6.66 mHz, corresponding to periods of 150–600 s) ULF waves observed by multiple spacecraft on 8 December 2013. The IMF was mostly northward. The two reasons for choosing this event are (1) for good satellite conjunction that provides observations in both the magnetosphere and the magnetosheath at the dusk MLTs and (2) for relatively steady solar wind conditions. Enhanced Pc5 perturbations were observed simultaneously in the inner magnetosphere, the plasma sheet, and the magnetosheath within the same narrow frequency ranges, suggesting that these magnetospheric waves were externally driven. Additionally, observations from ground magnetometers are used to investigate dawn-dusk asymmetries of these ULF waves. This paper is organized as follows. Instruments and measurements of these satellites are described in section 2. In section 3, we give an overview of the solar wind/IMF conditions and ULF waves observed in space and on the ground. In section 4, we present analysis of these waves and investigate their likely external drivers.

2. Data

In this study, we use observations from different satellite missions, including Time History of Events and Macroscale Interactions during Substorms (THEMIS), Van Allen Probes, Geotail, Cluster, Advanced Composition Explore (ACE), Acceleration Reconnection Turbulence and Electrodynamics of Moon's Interaction with the Sun (ARTEMIS), and Geostationary Operational Environment Satellites (GOES). For observations inside the magnetosphere but outside the plasmasphere, we use plasma and electric and magnetic field measurements from THEMIS E (TH-E for abbreviation) and from Van Allen Probes A and B (RBSP-A and RBSP-B for abbreviation), and magnetic field data from GOES 13. THEMIS probes cover regions inside $r \sim 12\ R_E$ with a period of ~23 h. The spin-fit magnetic field vectors of 3 s resolution measured by the FluxGate Magnetometer (FGM) instrument [*Auster et al*., 2008] and spin-fit electric field vectors (using $E \cdot B = 0$) of 3 s resolution measured by the Electric Field Instrument (EFI) [*Bonnell et al*., 2008] are used. The procedure of validating EFI data for ULF waves is described in Appendix A of *Hartinger et al.* [2012]. THEMIS provides particles and plasma moments with 3 s resolution measured by the electrostatic analyzer (ESA, 0.006–20 keV/q for ions and 0.007–26 keV for electrons) [*McFadden et al*., 2008] and the Solid State Telescope (SST, 35 keV–6 MeV for ions and 30 keV–6 MeV for electrons). Plasma pressure is a summation of ion and electron pressures from both ESA and SST pressures. The apogee for the Van Allen Probes spacecraft is ~5.8 R_E with orbit periods ~9 h. Magnetic field vectors of ~4 s resolution measured by the Electric and Magnetic Field Instrument Suite and Integrated Science (EMFISIS) [*Kletzing et al*., 2013] and corotation frame spin-fit electric field vectors (using $E \cdot B = 0$) of ~10 s resolution measured by the Electric Field and Waves Instrument (EFW) [*Wygant et al*., 2013] are used. For Van Allen Probes, valid $E \cdot B = 0$ approximation requires that the angle between spacecraft spin axis and magnetic field vector is less than 75° (detailed explanation is described in the required reading page for EFW data, http://www.space.umn.edu/rbspefw-data-policy-the-rules-of-the-road/). For the time interval we investigated, the angles for both RBSP-A and RBSP-B remained smaller than 75°. Van Allen Probes provides particles and plasma moments [*Spence et al*., 2013] measured by the Helium Oxygen Proton Electron (HOPE) instrument (0.001 to 50 keV for H^+, He^+, O^+ ions, and electrons) [*Funsten et al*., 2013] and the Magnetic Electron Ion Spectrometer (MagEIS) instrument (30 keV to 4 MeV for electrons and 20 keV to 1 MeV for ions) [*Blake et al*., 2013]. Plasma pressure is a summation of ion and electron

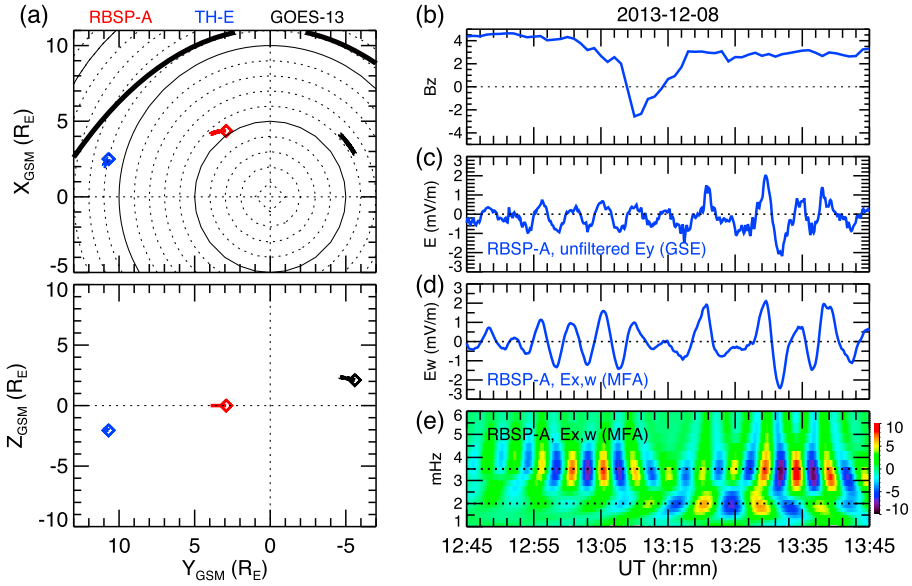

Figure 1. (a) *X-Y* (top) and *Y-Z* (bottom) projections of the trajectories of different satellites from 12:45 to 13:45 UT on 8 December 2013, with the square symbol indicating their locations at 12:45 UT. The thick black line is magnetopause location predicted by the Roelof and Sibeck model [*Roelof and Sibeck*, 1993] for the solar wind dynamic pressure = 2 nPa and IMF B_z = 2 nT. (b) IMF B_z from OMNI. (c) Unfiltered E_y component in GSE coordinates, (d) E_x perturbations in MFA coordinates (the subscript "w" in this paper indicates perturbation), and (e) the real part of the Morlet wavelet spectrum of the E_x perturbations observed by RBSP-A.

pressures from both HOPE and MagEIS pressures. Note that there is a small uncertainty in the ion plasma pressure because all ions are assumed to be protons, but this uncertainty is not expected to affect the analysis results in this study. GOES 13 magnetic field vectors with 1 min resolution measured by the fluxgate magnetometer [*Singer et al*., 1996] are used.

Measurements from Geotail and Cluster are used for the observations in the magnetosheath. For Geotail, particle and plasma moments with 12 s resolution measured by the low-energy particle (LEP) instrument [*Mukai et al*., 1994] (0.021 to 44 keV/*q* for ions and 0.043 to 41 keV for electrons) and magnetic field vectors with 12 s resolution measured by the magnetic field experiment [*Kokubun et al*., 1994] are used. For Cluster, proton moments (0.05–32 keV) with 4 s resolution measured by the Cluster Ion Spectrometry/Composition and Distribution Function Analyser (CIS/CODIF) [*Rème et al*., 2001] and magnetic field vectors of 4 s resolution measured by the FluxGate Magnetometer (FGM) instrument [*Balogh et al*., 2001] are used.

For the solar wind and IMF conditions, we use 1 min OMNI solar wind and IMF data [*King and Papitashvili*, 2005]. The data have been time shifted to the Earth's bow shock nose. In addition, we also use 1 s resolution IMF data measured by ACE [*Smith et al*., 1998] and solar wind/IMF observed by ARTEMIS. ARTEMIS instruments are the same as THEMIS. For the ground magnetic field measurements, we use magnetic field vectors with 1 min resolution provided by SuperMAG [*Gjerloev*, 2009]. SuperMAG generates validated magnetic field perturbations from more than 300 ground magnetometers with all data being rotated into the same geomagnetic coordinate system (north (*H*), east (*D*), and down (*Z*)) and with a common baseline removal [*Gjerloev*, 2012].

3. ULF Waves in the Magnetosphere

3.1. Event Overview

We investigate a magnetospheric Pc5 ULF wave event observed at two radial distances. The event was during a quiet period from 12:45 to 13:45 UT on 8 December 2013. Figure 1a shows the *X-Y* and *Y-Z* projections of RBSP-A, TH-E, and GOES 13. RBSP-A was in the duskside inner magnetosphere at $r \sim 5\ R_E$ and was outside the plasmapause (the number density estimated from the spacecraft potentials was ~10–20 cm^{-3}). TH-E

was in duskside the plasma sheet at $r \sim 11\ R_E$. The Alfvén speed was ~900 km/s at RBSP-A and ~1700 km/s at TH-E, and plasma beta at these two locations were ~0.1 to 0.2. GOES 13 was in the dawnside inner magnetosphere. This event was in the recovery phase of a moderate storm (its main phase started at ~03 UT and the recovery phase started at ~0830 UT as determined from the *Dst* minimum of ~ −70 nT). *Dst* was ~ −40 nT and *AE* was < ~100 nT. Figure 1b shows that IMF B_z was mostly northward during this event. The solar wind density, speed, and dynamic pressure all remained relatively steady. The solar wind speed (~620 km/s) was high, which is within the fast solar wind regime.

Figure 1c shows unfiltered electric field observed in the inner magnetosphere by RBSP-A. In this event, we focused on the large fluctuations of periods of a few to ~10 min seen in electric and magnetic fields. We thus detrended the unfiltered data by subtracting 15 min running averages and also filtered out perturbations with frequencies higher than 8.3 mHz by applying 1 min smoothing. For the waves observed in the magnetosphere, we transformed field components to mean-field-aligned (MFA) coordinates. The Z_{MFA} component is in the direction of the background magnetic field determined from 15 min running averages, the Y_{MFA} component is the cross product of the spacecraft's position unit vector and Z_{MFA} and it points azimuthally eastward (so the positive Y_{MFA} is pointed eastward), and the X_{MFA} component completes the orthogonal right-hand system (so positive X_{MFA} is pointed outward). Magnetic field perturbations in Z_{MFA} indicate compressional waves. Transverse magnetic perturbations in X_{MFA} indicate poloidal or radial components, while those in Y_{MFA} indicate toroidal or azimuthal components. Figure 1d shows RBSP-A electric field perturbations obtained from the above processing and Figure 1e shows the real part of the Morlet wavelet spectrum of the perturbations.

Electric field fluctuations with amplitudes up to ~3 mV/m were observed by RBSP-A. From ~12:45 to 13:15 UT (referred to as "the first interval"), both the unfiltered and detrended data show electric field fluctuations with periods of ~4–5 min, which matches the enhancement in ~3.5 mHz shown in the wavelet spectrum. From ~13:15 to 13:45 UT (referred to as "the second interval"), fluctuations were enhanced and, in addition to the 3.5 mHz fluctuations, enhancement in a second frequency of ~2 mHz also appeared. Power amplification in magnetic fields were also seen in similar frequency ranges of ~3.5–4 mHz and ~1.5–2 mHz. Fluctuations in these two frequency bands were also observed in the plasma sheet by TH-E. These two frequency bands are within the Pc5 range. Wave amplification in these two separate frequency bands suggests that they might be driven by different drivers. In the following we investigate the wave characteristics and their likely drivers separately for the first and second intervals.

3.2. Waves During the First Interval

Pc5 waves observed in space and on the ground during the first interval are shown in Figure 2. Figure 2a shows that electric field oscillations in the 3.5–4 mHz band were observed simultaneously by RBSP-A and TH-E, and the E_x oscillations at RBSP-A (with the peaks indicated by the vertical purple lines) were approximately in phase with the E_y oscillations at TH-E. Electric field polarization at both RBSP-A and TH-E locations were similar with a ~ 90° phase difference between E_x and E_y. RBSP-B, which was at a similar radial distance as RBSP-A but ~2 R_E away azimuthally, also observed electric field perturbations in the same frequency band but with substantially smaller amplitudes (not shown). Figure 2b shows that for the perturbations in the transverse magnetic field components B_x and B_y, the same counterclockwise polarization was observed at both the RBSP-A and TH-E locations. These spatial differences suggest that the 3.5–4 mHz transverse electric and magnetic field perturbations have a large radial extent but a limited azimuthal extent. In contrast to the transverse components, fluctuations in the compressional magnetic field shown in Figure 2c at these two radial distances were irregular and not clearly correlated with each other. The $E \times B$ flow perturbations, as shown in Figures 2d and 2e, were found to have the same counterclockwise rotations in both the inner magnetosphere (RBSP-A) and the plasma sheet (TH-E) throughout this interval. Figure 2f shows GOES 13 magnetic field perturbations on the dawnside; the 3.5–4 mHz fluctuations were seen in the transverse magnetic field but not in the compressional magnetic field, similar to those observed by RBSP-A. Figure 2g shows that the 3.5–4 mHz band fluctuations were observed on the ground on both the duskside and dawnside at lower auroral latitudes (the equatorial location was $X \sim 2$ and $Y \sim 5\ R_E$ for the SOD station and $X \sim 1$ and $Y \sim -5\ R_E$ for the ISL station based on the Tsyganenko 01 (T01) magnetic field model [*Tsyganenko*, 2002a, 2002b]).

The above perturbation enhancements in the same frequency band observed at two different radial distances with a large separation (at $r \sim 5$ and 11 R_E) are not consistent with the excitation of field line

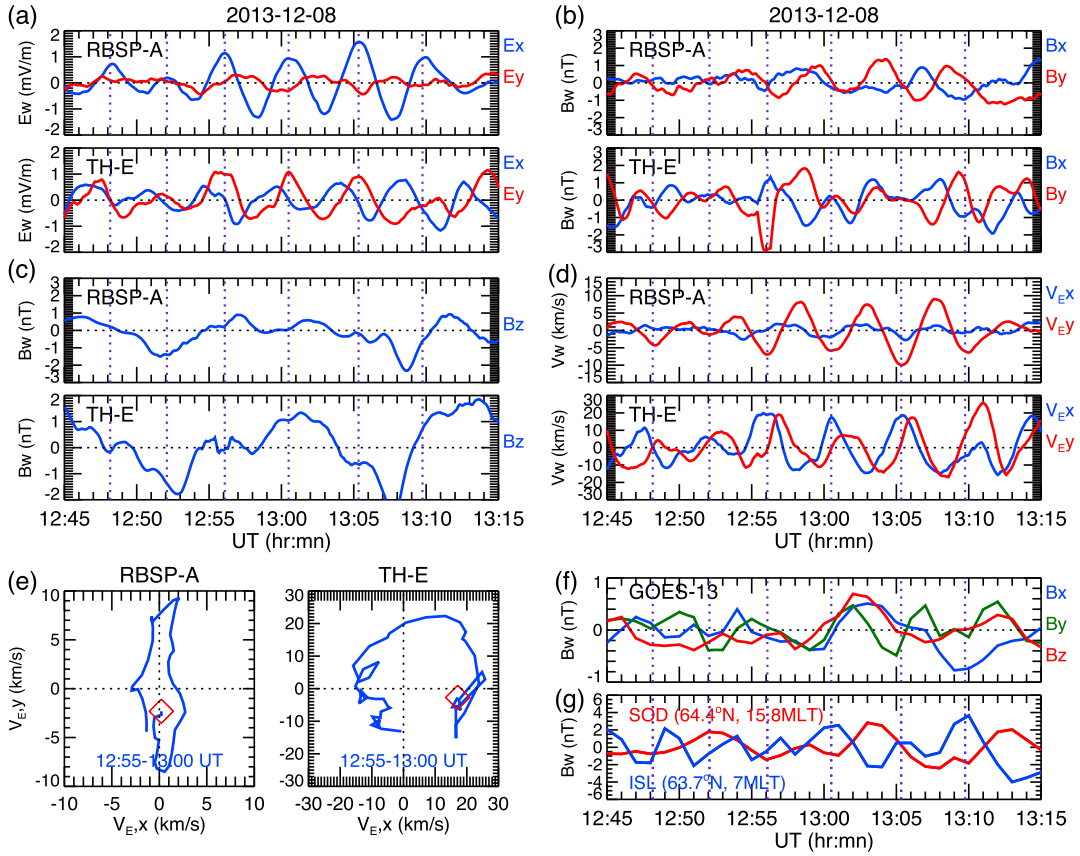

Figure 2. Perturbations in (a) the E_x and E_y components, (b) B_x and B_y components, (c) B_z component, and (d) X and Y components of $\mathbf{E} \times \mathbf{B}$ flows in MFA coordinates observed by RBSP-A and TH-E during the first interval. (e) Hodogram of the flow perturbations from 12:55 (red squares) to 13:00 UT observed by RBSP-A (left) and TH-E (right). (f) Magnetic field perturbations in MFA coordinates observed by GOES 13. (g) Ground magnetic field perturbations in the H component observed at stations SOD and ISL.

resonances (FLRs) [*Tamao*, 1965]. The FLR mechanism predicts that transverse magnetic waves are excited at a location where the field line shell eigenfrequency equals the frequency of compressional magnetic waves, and radially across that location the phases of the toroidal (B_y) component are 180° out of phase and the polarization directions are reversed [e.g., *Nishida*, 1978]. As shown in Figures 2a and 2b, this predicted FLR polarization change is also not observed at the two locations. The transverse perturbations are unlikely driven by a cavity mode [*Kivelson and Southwood*, 1986]; if that was the case, E_y and B_z would be ~90° out of phase [e.g., *Hartinger et al.*, 2012]. The transverse perturbations are also unlikely to be driven by a waveguide mode [*Samson et al.*, 1992]; in the presence of a waveguide mode, significant changes in transverse magnetic field polarization are expected to change over small (on order of 1 R_E) radial distance [e.g., *Rickard and Wright*, 1995], whereas the same polarizations were observed across roughly 6 R_E. Furthermore, the low plasma beta values at the RBSP-A and TH-E locations (~0.1–0.2) were not favorable for waves driven by plasma instabilities in high beta plasma, such as drift compressional instability [*Hasegawa*, 1971]. As discussed in sections 4.1 and 5, the observed electric field and flow perturbations can be explained by with large flow vortical structures driven by magnetopause surface waves.

3.3. Waves During the Second Interval

Figure 3 shows the perturbations observed during the second interval. Comparing with the perturbations during the first interval, the perturbations during the second interval were stronger, but they were more complicated as fluctuation amplitudes of the 1.5–2 and 3.5–4 mHz bands were comparable, making it more difficult to discriminate between them in time series. Figure 3a shows that both RBSP-A and TH-E observed large B_z perturbations starting at ~13:16 UT. The 1.5–2 mHz band fluctuations had substantially larger

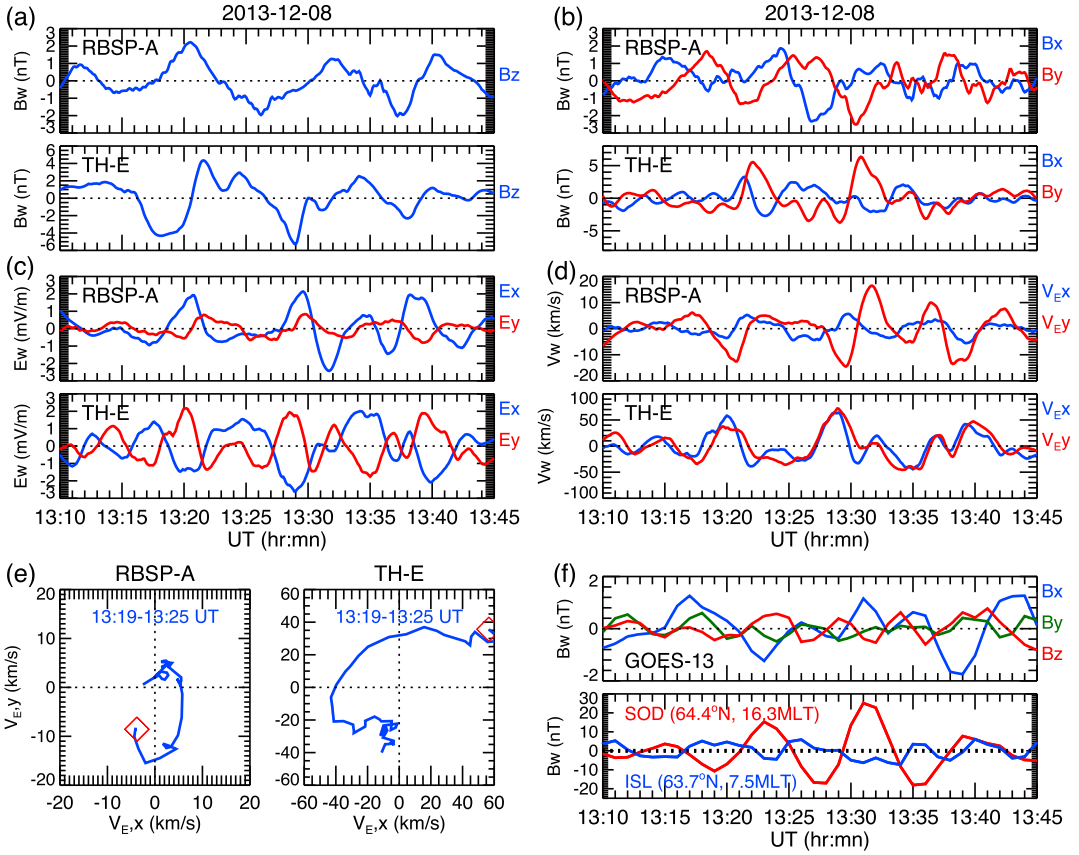

Figure 3. Perturbations in the (a) B_z component, (b) B_x and B_y components, (c) E_x and E_y components, and (d) V_x and V_y components in MFA coordinates observed by RBSP-A and TH-E during the second interval. (e) Hodogram of the flow perturbations from 13:19 (red squares) to 13:25 UT observed by RBSP-A (left) and TH-E (right). (f) Magnetic field perturbations in MFA coordinates observed by GOES 13. (g) Ground magnetic field perturbations in the *H* component observed at stations SOD and ISL.

amplitudes than the 3.5–4 mHz band fluctuations throughout this interval. Figure 3b shows the transverse magnetic field perturbations, and it can be seen that at both spacecraft locations the amplitudes of the 1.5–2 mHz band were substantially larger than those of the 3.5–4 mHz band. The magnetic field polarization directions in the inner magnetosphere (RBSP-A) and the plasma sheet (TH-E) were both counterclockwise. Figure 3c shows that the 1.5–2 mHz electric field perturbations were substantially stronger than those of 3.5–4 mHz in the inner magnetosphere, while in the plasma sheet their amplitudes were more comparable to each other. Comparing the amplitudes between these two frequency bands as a function of radial distances shows that the enhancements in the 1.5–2 mHz band were similar in both the plasma sheet and the inner magnetosphere, while enhancements in the 3.5–4 mHz band were larger in the plasma sheet than the inner magnetosphere. As a result, the 1.5–2 mHz perturbations were larger than the 3.5–4 mHz perturbations in the inner magnetosphere. Figures 3d and 3e show that the initial flow perturbations rotated counterclockwise in both the inner magnetosphere and plasma sheet, but later the flow pattern became complicated as the perturbation amplitudes from these two competing frequency bands became comparable. Interestingly, in contrast to the strong enhancement in the B_z perturbations seen on the duskside, Figure 3f shows that GOES 13 on the dawnside observed no such B_z enhancement. Similar dawn-dusk asymmetry was also seen on the ground, as Figure 3g shows that enhancement in the *H* component was much stronger on the duskside than on the dawnside. As discussed in section 4.2, the dawn-dusk asymmetry can be explained by a dawn-dusk asymmetric external driver.

For the enhancement in the 1.5–2 mHz magnetic field perturbations during the second interval, Figure 3a shows that compressional waves were seen from the plasma sheet to the inner magnetosphere and Figure 3b shows that B_y at the RBSP-A location was ~180° out of phase with B_y at the TH-E location.

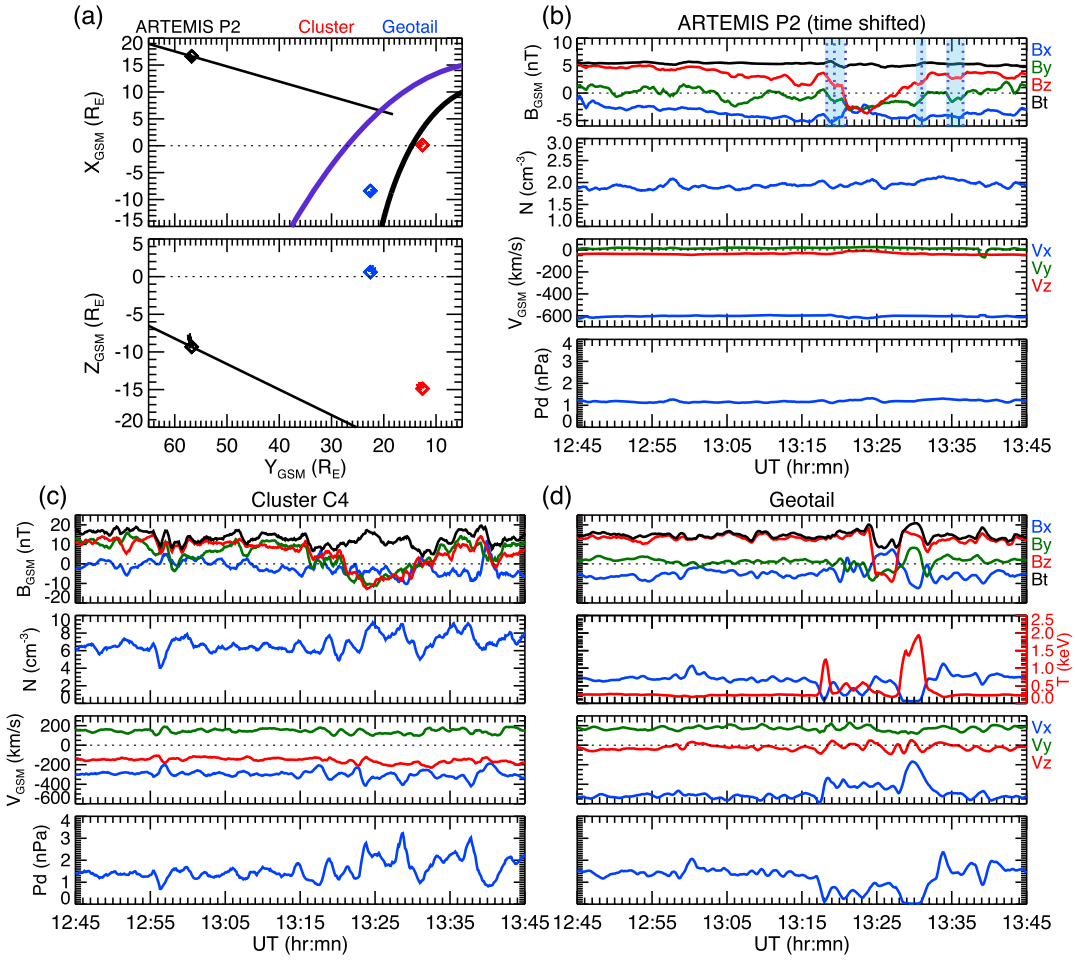

Figure 4. (a) *X-Y* (top) and *Y-Z* (bottom) projections of the trajectories of different satellites, with the square symbol indicating their locations at 12:45 UT. The thick black line is magnetopause location at $Z = 0$ predicted by the Roelof and Sibeck model [*Roelof and Sibeck*, 1993] for the solar wind dynamic pressure = 2 nPa and IMF $B_z = 2$ nT. The thick purple line is bow shock location at $Z = 0$ predicted by the model of *Peredo et al.* [1995] for observed Mach number = 9. The thin black line crossing ARTEMIS indicates the IMF discontinuity discussed in section 4.2. Magnetic field components, number density, flow velocities, and dynamic pressure observed by (b) ARTEMIS P2, (c) Cluster C4, and (d) Geotail. The magnetic field and velocities are in GSM coordinates. The ARTEMIS data have been time shifted (see text). The vertical dotted lines in Figure 4b indicate IMF discontinuities. Ion temperature observed by Geotail is overplotted on top of Geotail number density.

However, the polarization directions at these two locations were the same and the enhancement was observed over such a large radial distance range that it cannot be explained by FLRs. On the other hand, for many of these B_z perturbations observed by RBSP-A, there was a phase difference close to 90° from the E_y perturbations. This phase difference may suggest standing compressional waves trapped between the magnetopause and the plasmapause that are associated with the cavity/waveguide modes.

4. External Drivers

In this section we investigate the solar wind and magnetosheath observations for likely external drivers for the magnetospheric ULF waves observed during the two intervals. Figure 4 shows observations from ARTEMIS P2 in the solar wind, and from Cluster C4 and Geotail in the magnetosheath. As shown in Figure 4a, both Cluster and Geotail were on the duskside with Cluster at high latitudes in the Southern Hemisphere and Geotail at low latitudes. Geotail later encountered plasma sheet plasma in magnetopause boundary layer from ~13:17 to 13:33 UT as indicated by appearance of hot (> 1 keV) and tenuous (< 1 cm^{-3}) plasma. All of these satellites observed a brief and sharp magnetic field change to southward,

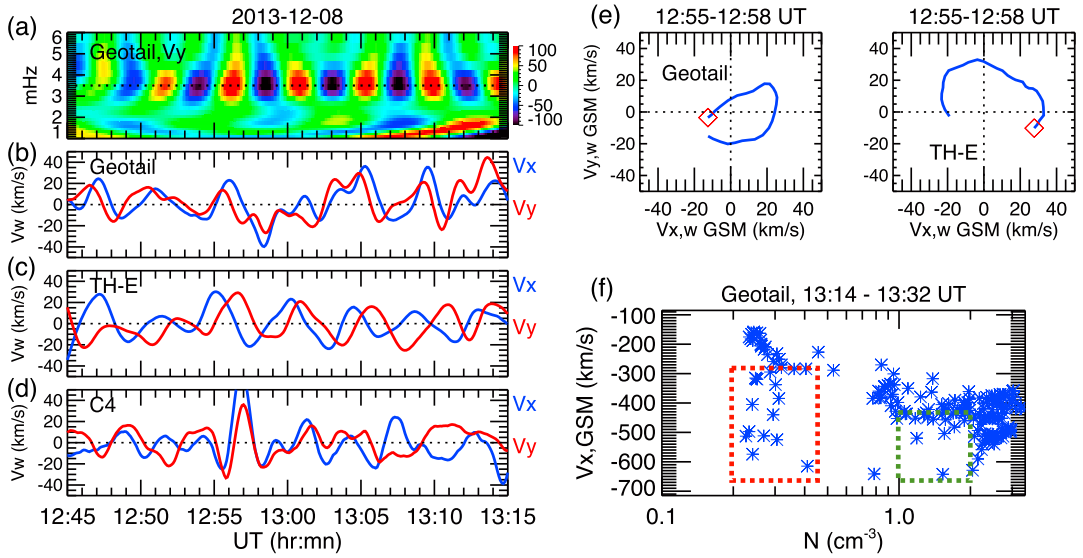

Figure 5. (a) The real part of Morlet wavelet spectrum of V_y perturbations in GEM coordinates observed by Geotail. V_x and V_y perturbations in GSM coordinates observed by (b) Geotail, (c) TH-E, and (d) Cluster C4. (e) Hodogram of the flow perturbations from 12:55 (red squares) to 12:58 UT observed by Geotail (left) and TH-E (right). (f) Ion number density versus velocity in the *X* direction observed by Geotail from 13:14 to 13:26 UT during the encounter of magnetopause boundary layer. The green (red) dotted rectangle indicates the lower-density and higher-velocity feature in plasma of plasma depletion layer (plasma sheet).

indicating the observed pristine solar wind/IMF structures indeed impacted the Earth. For better comparisons, we shifted the ARTEMIS time series by shifting the time of B_z changing from positive to negative to 13:21 UT as observed by Cluster in the magnetosheath. In the solar wind, IMF strength, density, speed, and dynamic pressure were all relatively steady with variations less than 10% and most importantly the solar wind dynamic pressure showed no strong fluctuations in the 1.5–2 mHz and 3.5–4 mHz bands. This suggests that the magnetospheric ULF waves were not driven by the solar wind dynamic pressure perturbations. The magnetosheath pressure was higher in the parallel than in the perpendicular direction by a factor of <1.5 during most of the first interval, which was not a favorable condition for mirror and proton cyclotron instabilities. The MHD firehose parameter, $1–0.5(\beta_{||}–\beta_{\perp})$ [e.g., *Siscoe*, 1983] was found to be larger than 0, so it was also unfavorable to firehose instability. Despite that the density and flows were steady in the solar wind, there were clear Pc5 perturbations in magnetosheath density, magnetic field, and flows during the second interval. The magnetosheath pressure anisotropy was weak at the time. Even though mirror and cyclotron modes could produce large density and magnetic field variations, they are normally observed in the Pc3 (22–100 mHz) range. Also, the anticorrelation between density and magnetic field variations for mirror mode waves was not observed in our event. This suggests that the density perturbations may be generated near the foreshock region. We further investigate these magnetosheath perturbations in detail and their connection with the magnetospheric ULF waves during the two intervals.

4.1. External Driver During the First Interval

Figure 5a shows the real part of Morlet wavelet spectrum of magnetosheath flow perturbations observed by Geotail during the first interval. The flow fluctuated in ~3.5 mHz, the same as the magnetospheric waves observed during the first interval. Figures 5b and 5c compare the flow perturbations observed by Geotail and TH-E in GSM coordinates (Geotail spacecraft speed was less than 1 km/s). The flow rotated clockwise in the magnetosheath but counterclockwise inside the magnetosphere. This flow rotation pattern on the opposite sides of the magnetopause shown in Figure 5e suggests that the flow perturbations were likely caused by tailward propagating surface waves [*Plaschke et al.*, 2014]. Cluster C4 in higher-latitude magnetosheath observed flow perturbations in a slightly higher frequency of ~4.5 mHz. However, as shown in Figure 5d, comparing with the Geotail flows, the Cluster flow fluctuations were weaker and did not have coherent flow rotation. This suggests that the surface waves were excited near the equatorial

magnetopause. Considering that the northward IMF and high solar wind speed during this interval should provide favorable conditions for unstable K-H waves, we use the measurements of Cluster C4 (at $X_{GSM} \sim 0$) in the magnetosheath side and TH-E (at $X_{GSM} \sim 2\ R_E$) in the magnetosphere side to make a crude evaluation of the K-H instability condition [*Chandrasekhar*, 1961]:

$$((\mathbf{V}_1 - \mathbf{V}_2)\cdot\mathbf{k})^2 > \frac{1}{\mu_0 m_i}\left(\frac{1}{n_1}+\frac{1}{n_2}\right)\left[(\mathbf{k}\cdot\mathbf{B}_1)^2 + (\mathbf{k}\cdot\mathbf{B}_2)^2\right] \quad (1)$$

where **V** is velocity vector, **k** is the wave vector, n is number density, **B** is magnetic field vector, m_i is proton mass, and subscripts 1 and 2 refer to magnetosheath and magnetosphere quantities, respectively. To obtain better estimation of the magnetosheath values along the magnetopause surface, we transferred Cluster magnetic field and velocity components to local magnetopause coordinates, LMN, in which **N** is pointed outward along the normal to the magnetopause (determined from the Roelof and Sibeck model [*Roelof and Sibeck*, 1993], as shown in Figure 4a), **M** is determined by $\mathbf{z}_{GSM} \times \mathbf{N}$ (positive **M** is tailward), and **L** is determined by $\mathbf{N} \times \mathbf{M}$. With the assumption of axisymmetric magnetosheath distributions, the observations suggest that the conditions across the equatorial magnetopause, for example, at 12:43 UT, were $V_{1M} = -313$ km/s, $n_1 = 6.2$ cm^{-3}, $B_{1L} = 15.4$ nT, $B_{1M} = 6.4$ nT, $V_{2M} = -17$ km/s, $n_2 = 0.53$ cm^{-3}, $B_{2L} = 36$ nT, and $B_{2M} = 0$. Because magnetic field was not zero along the shear, the **k** for maximum growth phase is expected to be tilted from the flow shear plane [*Nakamura et al*., 2006; *Eriksson et al*., 2016], and its direction at the time was $k_L = -0.05$, $k_M = -0.998$, and $k_N = 0$ as estimated by using equation (4) of *Nakamura et al.* [2006]. The unstable condition in equation (1) was satisfied with these values. We examined the observations at different times from ~12:40 to 12:44 UT before the wave enhancement and found that the cross-magnetopause conditions were K-H unstable; therefore, the surface waves could possibly be driven by K-H instability.

At this time Geotail was not right at the magnetopause so there is no direct evidence for K-H waves. However, as shown in Figure 4d, Geotail later encountered the magnetopause boundary layer between ~13:17 and 13:33 UT and observed plasma from the plasma depletion layer [*Sibeck et al*., 1990] as well as from the plasma sheet. Plasma depletion layer is outside the magnetopause and is characterized by decreased density and increased magnetic field strength compared to the magnetosheath. Figure 5f shows Geotail density versus flow in the X_{GSM} direction during the encounter of the magnetopause boundary layer. Besides observing typical low-density and low-velocity magnetosphere plasma and high-density and high-velocity magnetosheath plasma, Geotail also observed a lower-density and higher-velocity feature in plasma of the plasma depletion layer (the plasma of this feature is approximately indicated by the green dotted rectangle) and also in plasma sheet plasma (as indicated by the red dotted rectangle). This feature in the plasma depletion layer can be explained by plasma being accelerated by surface waves that may or may not be driven by K-H instability [*Plaschke et al*., 2014]. But this feature seen in plasma sheet plasma has been shown in simulations [*Takagi et al*., 2006] to be accelerated exclusively by a rolled-up vortex of K-H-driven surface waves. This feature has been commonly used in many studies with single-satellite observations as an indication for the occurrence of a K-H vortex [e.g., *Hasegawa et al*., 2006; *Hwang et al*., 2011; *Taylor et al*., 2012]. With this additional indirect evidence, K-H surface waves are plausibly the external driver for the 3.5–4 Hz magnetospheric ULF waves observed during the first interval. In section 5, we compare the observed ULF perturbations with predicted ULF wave signatures from a MHD simulation of K-H surface wave [*Claudepierre et al*., 2008].

4.2. External Driver During the Second Interval

Figure 6 shows the magnetosheath observed by Cluster and Geotail. Figure 6a shows that for each dip in the magnetosheath dynamic pressure observed by Cluster, as indicated by red arrows, there was a corresponding decrease in the density observed by Geotail, as indicated by blue arrows. From the appearance of keV electrons, the first four Geotail density decreases were due to encounters of plasma sheet plasma in the magnetopause boundary layer. The last density decrease at ~1340 UT was accompanied by an increase of magnetic field strength but no hot plasma sheet electrons, indicating an encounter with only the plasma depletion layer. The good correspondence with the deceases in the magnetosheath dynamic pressure thus suggests that these encounters are due to outward deformation of the magnetopause. Figure 6b shows filtered magnetosheath dynamic pressure fluctuations in the 1.5–2 mHz (band 1) and 3.5–4 mHz (band 2) bands observed by Cluster in comparison with electric and magnetic field perturbations in the

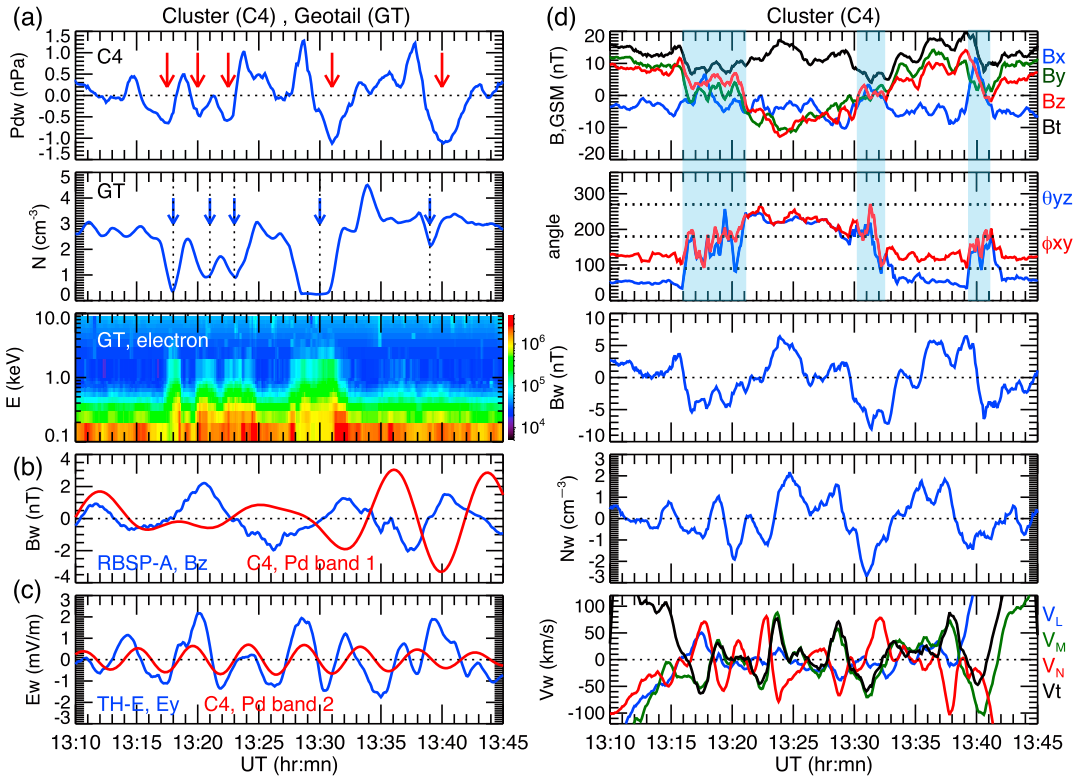

Figure 6. (a) From top to bottom: dynamic pressure perturbations observed by Cluster C4, density and electron energy flux (1/(s sr cm^2)) observed by Geotail. (b) Comparison of B_z perturbations observed by RBSP-A with the dynamic pressure perturbations at the 1.5–2 mHz band (band 1) observed by Cluster C4 ($P_{d,w}$ is multiplied by a factor of 5 for better visualization). (c) Comparison of E_y perturbations observed by TH-E with the dynamic pressure perturbations at the 3.5–4 mHz band (band 2) observed by Cluster C4 ($P_{d,w}$ is multiplied by a factor of 2). (d) From top to bottom: magnetic field components in GSM coordinates, angles between B_y and B_z (θ_{yz}) and between B_x and B_y (ϕ_{xy}), and fluctuations of magnetic field strength, density, and flows in LMN coordinates observed by Cluster C4.

magnetosphere (note that the magnitudes of pressure perturbations have been scaled for better visualization of the comparison). The 1.5–2 mHz band, which corresponded to the dynamic pressure dips, were out of phase with the B_z perturbations in the inner magnetosphere observed by RBSP-A (see Figure 3a). On the other hand, the 3.5–4 mHz band, which corresponded to the pressure peaks, were approximately in phase with the E_y perturbations in the plasma sheet observed by TH-E (see Figure 3c) before 13:30 UT (note that the B_z perturbations at the TH-E location were dominated by the 1.5–2 mHz band). The above direct correspondences indicate that it was the external forcing of magnetosheath dynamic pressure perturbations on the magnetopause that drove those ULF waves in the magnetosphere during the second interval.

As shown in Figure 4b, in comparison with the first interval, during the second interval the IMF magnitude, the solar wind density and speed, and the solar wind dynamic pressure remained similar and also relatively steady, but there were a few changes in the IMF direction. Several of these IMF direction changes were associated with IMF discontinuities as indicated by vertical dotted lines (these IMF discontinuities were also observed by ACE at (233, 42, 12) R_E, not shown). The discontinuity normal is determined using minimum variance analysis [*Sonnerup and Scheible*, 1998] requiring that the minimum-to-intermediate eigenvalue ratio be less than 0.1 [*Liu et al.*, 2015] and checked with the cross product method [*Schwartz*, 1998] if magnetic field along the discontinuity normal is close to zero. A discontinuity is defined here to have a direction change larger than 20° within 1 min. A chain of discontinuities were observed by both ACE and ARTEMIS and they were clustered in three bunches as indicated by shaded light blue in Figure 4b. Figure 6d shows the magnetosheath magnetic field and plasma parameters observed by Cluster. It can be seen that there were also three bunches of substantial magnetic field direction changes in the magnetosheath (shaded light blue), and they

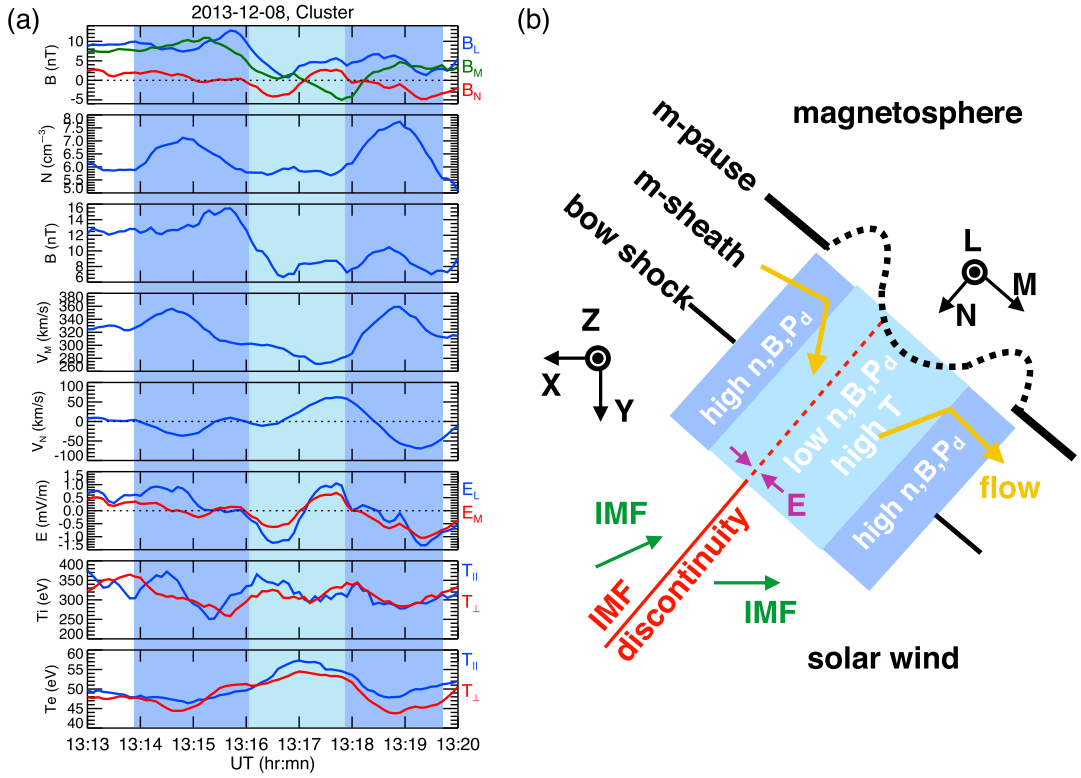

Figure 7. (a) A magnetosheath perturbation observed by Cluster C4. From top to bottom: magnetic field in LMN coordinates, number density, magnetic field strength, flow in the *M* direction, flow in the *N* direction, electric field in the *L* and *M* directions, ion temperature, and electron temperature (electron temperature from Cluster C2). (b) Schematic interpretation of the structure of the perturbation shown in Figure 7a.

matched the three bunches of IMF discontinuities with reasonable timing uncertainty from the solar wind to the magnetosheath, indicating that those IMF discontinuities have crossed the bow shock. Note that an IMF discontinuity may become less sharp in the magnetosheath so that the magnetosheath magnetic field direction change may no longer be qualified as a discontinuity.

In contrast to the approximately constant (variations <10%) IMF strength and number density across those IMF discontinuities observed by ARTEMIS, in the magnetosheath Cluster observed significant drops (up to ~50%) in both the magnetic field strength and number density and enhanced flows corresponding to the three bunches of magnetic field direction changes. As discussed at the beginning of section 4, these perturbations were not consistent with being generated by magnetosheath instabilities; we thus focus the investigation on perturbations originated around the bow shock. Their direct correspondences with IMF discontinuities thus suggest that they may be a result of transient ion foreshock perturbations generated by the kinetic interaction of IMF discontinuities with the quasi-parallel bow shock, such as hot flow anomalies (HFAs) [e.g., *Schwartz et al.*, 1985; *Thomsen et al.*, 1986; *Lucek et al.*, 2004; *Omidi and Sibeck*, 2007; *Zhang et al.*, 2010] and foreshock bubbles (FBs) [e.g., *Omidi et al.*, 2010; *Turner et al.*, 2013; *Liu et al.*, 2015]. As these perturbations propagate into the magnetosheath and move tailward, they can cause magnetopause deformation and enhanced ULF waves in the magnetosphere, and these geoeffects may be dawn-dusk asymmetric depending on the discontinuity normal direction [e.g., *Sibeck et al.*, 1999; *Jacobsen et al.*, 2009; *Archer et al.*, 2014, 2015]. Unfortunately, there was no spacecraft in the foreshock during this interval to provide direct evidence for foreshock perturbations being the cause of the observed magnetosheath perturbations. But as we show in the following, characteristics of the fluctuations in the magnetosheath and magnetosphere provide some supporting evidence. Figure 7a shows the observed changes in magnetic field and plasma parameters in LMN coordinates associated with the first magnetosheath perturbation shown in Figure 6d, and Figure 7b shows a schematic interpretation of the structure of that perturbation. There was a magnetic field direction change across this perturbation. This perturbation consisted of a core

region (shaded in light blue in both Figures 7a and 7b) with lower density and magnetic field strength enclosed by two edges of higher density and magnetic field strength (shaded in light purple). Flow speed decreased in the *M* direction (along the magnetopause), while the flow in the *N* direction (normal to the magnetopause) changed signs, indicating that the tailward magnetosheath flow was diverted around the perturbation. The motional electric field ($\mathbf{E} = -\mathbf{V} \times \mathbf{B}$) was pointed toward the center of the magnetic field change at 13:17 UT. There were increases in both ion and electron temperatures across the perturbation with the electron temperature increase more confined within the core region (the electron temperature was from Cluster C2 which was ~0.5 R_E from Cluster C4 because at the time electron temperature from C4 was not available). These changes resemble characteristically the features of HFAs and FBs observed in the foreshock region [*Schwartz et al.*, 1985; *Lucek et al.*, 2004; *Turner et al.*, 2013].

There was a delay from Cluster to Geotail in observing the first perturbation. Cluster at (0.29, 13, −14.5) R_E observed the peak of flow enhancement associated with the first perturbation at ~13:14:30 UT, while Geotail at (−8.6, 22.3, 0.9) R_E observed it ~3 min later at ~13:17:30 UT. This delay may be explained by a HFA perturbation propagating downstream with a speed determined by the solar wind speed parallel to the discontinuity normal. The solar wind velocity observed by ARTEMIS P2 at the time was (−596, 19, −33) km/s, and the normal direction for the IMF discontinuity at 13:18:20 UT was ~(−0.75, 0.21, 0.62) with 10% uncertainty as estimated from minimum variance analysis (similar values were also obtained from the ACE IMF). If we consider this discontinuity to be the driver of the first magnetosheath perturbation and we assume that it has the same discontinuity normal direction extending from ARTEMIS's location to outside the bow shock (see the black line in Figure 4a), then a delay of ~4 min from Cluster to Geotail is expected. This is reasonably consistent with the observed delay considering the uncertainties due to the estimation of normal direction.

In addition, typical scale sizes are a few R_E for HFAs and 5–10 R_E for FBs [*Facskó et al.*, 2009; *Turner et al.*, 2013], and they may have a stronger impact on ULF waves on one side of the magnetosphere than the other [*Hartinger et al.*, 2013] depending on the discontinuity normal direction. During the second interval the IMF was dominantly radial but was leaned more toward the duskside as indicated by the IMF B_x and IMF B_y shown in Figure 4b, and the normal directions of those IMF discontinuities were pointed duskward. These orientations should guide foreshock perturbations to move along the duskside, in agreement with the wave enhancement being observed on the duskside magnetosphere shown in Figure 3. Based on the above consistencies, a plausible interpretation for the ULF wave enhancement during the second interval is that a chain of IMF discontinuities as observed by ARTEMIS interacted with the foreshock and created transient foreshock perturbations, and as these perturbations propagated downstream along the duskside with their driver discontinuities they subsequently caused the magnetosheath dynamic pressure perturbations (observed by Cluster), which deformed the magnetopause (observed by Geotail) and thus generated ULF waves inside the duskside magnetosphere (observed by THEMIS, Van Allen Probes, and ground magnetometers).

5. Discussion

Repetitive or quasiperiodic magnetopause surface waves can be either caused by the solar wind disturbances with corresponding periods, by foreshock origin perturbations, by instabilities in the magnetosheath, or by instabilities at the magnetopause with periods determined by the instability growth rates [e.g., *Hwang and Sibeck*, 2016]. For the 3.5–4 mHz perturbations observed during the first interval, this characteristic period was only observed in low-latitude magnetosheath (Geotail) and magnetosphere (RBSP-A and TH-E) but not in the solar wind (ARTEMIS P2). There were only very weak broadband ULF fluctuations in the solar wind at the time. No strong density and magnetic field fluctuations in the magnetosheath during the first interval to suggest foreshock perturbations and the magnetosheath conditions were found to be unfavorable to magnetosheath instabilities. These suggest that the 3.5–4 mHz waves were more likely generated by an instability at the low-latitude magnetopause than directly by the solar wind or magnetosheath fluctuations. But any small perturbations in the solar wind or magnetosheath can become a seed fluctuation for the magnetopause instability [*Hwang and Sibeck*, 2016].

Considering the K-H surface waves for the driver of ULF waves inside the magnetosphere, previous observational studies suggested that the magnetospheric ULF waves can result from coupling K-H waves with either waveguide mode [*Rae et al.*, 2005] or FLR mode [*Agapitov et al.*, 2009]. However, in our event no compressional

waves in the 3.5–4 mHz band and no waveguide and FLR modes were observed in the magnetosphere. Here we discuss another mechanism that attributes the magnetospheric ULF waves to the inner mode of the two K-H modes [*Lee et al*., 1981]. In the presence of a boundary layer extending inward from the magnetopause, two K-H modes can be generated: the outer mode is centered at the magnetopause and the inner mode is centered at the inner edge of boundary layer inside the magnetosphere. Perturbations in the magnetosheath and magnetosphere associated with these two K-H modes have been investigated in many studies using global MHD simulations with focuses on either flows [*Li et al*., 2012, 2013, *Merkin et al*., 2013] or electric and magnetic fields [e.g., *Claudepierre et al*., 2008; *McGregor et al*., 2014]. Despite that the simulation setups and the specified solar wind/IMF conditions were not the same in these simulations, all these studies show generation of the two K-H modes. *McGregor et al.* [2014] study showed that such K-H modes can be excited in the same frequency under either very weak or strong broadband ULF solar wind fluctuations. The observed ULF perturbations in electric field and flow but not in B_z shown in Figure 2 are characteristically consistent with the model predictions of the Claudepierre et al. and McGregor et al. studies. In their simulations, the vortical flow structure associated with the inner mode causes monochromatic electric field perturbations several R_E inside the magnetopause, while B_z perturbations of the same frequency are mainly created by the outer mode and are confined within a much narrower radial extent. This offers an explanation why in our event no compressional waves in the same frequency band as electric field and flow perturbations were observed in the inner magnetosphere. In this scenario, it is the inner flow vortices, not fast mode waves, that play the role of transporting energy inward. The Merkin et al. study indicated generation of field-aligned currents by the velocity shear [*Southwood and Kivelson*, 1991] of the vortices, which could explain the observed transverse magnetic field perturbations in the same 3.5–4 mHz band. In addition, while electric field perturbations can be driven deeper inside the magnetosphere, they have limited azimuthal extent that may depend on the spatial scale of individual K-H vortices. This may explain why the well-structured flow perturbations observed by RBSP-A were not observed by RBSP-B nearby. Furthermore, *Li et al.* [2013] showed that the simulated flow perturbations associated with the outer mode become weaker with increasing Z distances from the equatorial plane. This may explain the weaker flow perturbations and less coherent flow rotations observed by Cluster in high-latitude magnetosheath. However, the simulations did not investigate how the K-H frequency might vary in the Z direction and it remains to be understood why Cluster observed higher frequency of ~4.5 mHz.

On the other hand, global hybrid simulations of ion foreshock perturbations and their impact on the magnetosheath and magnetopause remain very limited [e.g., *Omidi et al*., 2016], and these simulations have not investigated the responses inside the magnetosphere. Therefore, no simulation results are available for comparing with the observed ULF waves during the second interval. In addition to HFAs and FBs, there exist many other types of perturbations initially generated near the foreshock, such as spontaneous HFAs [*Zhang et al*., 2013; *Omidi et al*., 2016], magnetosheath filamentary structures [*Omidi et al*., 2014], transient flux enhancements or jets [e.g., *Němeček et al*., 1998; *Hietala et al*., 2012], or large-scale low-frequency electromagnetic wavefronts [*Karimabadi et al*., 2014]. But these perturbations are less likely to be the cause of the magnetosheath perturbations during the second interval since their formation do not require IMF discontinuities and their associated variations are not consistent with those observed by Cluster. In the future more observation and simulation studies are needed to better understand how these foreshock perturbations evolve and interact in the magnetosheath as they propagate tailward to the nightside, as well as how they interact with other magnetopause perturbations such as K-H surface waves.

6. Summary

In this event study we use multiple spacecraft observations to investigate magnetospheric Pc5 ULF waves under steady solar wind and quiet geomagnetic conditions and their likely external drivers. Our key findings are the following:

1. Electric and magnetic field perturbations in two narrow frequency bands, 1.5–2 mHz and 3.5–4 mHz, were observed in the magnetosphere over a large radial distance range from r ~ 5 to 11 R_E. Perturbations in these two bands were also observed in the magnetosheath, but these perturbations were not driven by solar wind dynamic pressure perturbations.
2. During the first interval of this event, enhanced perturbations in the 3.5–4 mHz band were observed in the transverse electric and magnetic field components, and plasma flows. The enhancement occurred over a

large radial distance range but within a limited azimuthal region. The magnetic field polarization directions at $r = 5$ and 11 R_E were the same. No compressional waves in the 3.5–4 mHz band were observed, and the transverse magnetic field perturbations are not consistent with being excited by FLRs or cavity/waveguide modes. The flow oscillations in the magnetosheath and the magnetosphere were well correlated, and their rotation directions were opposite to each other. In addition, the hot and tenuous plasma sheet plasma in the magnetopause boundary layer had a flow signature associated with rolled-up K-H vortices. From qualitative comparisons with global MHD simulations of K-H waves, these electric field and flow ULF perturbations inside the magnetosphere during the first interval can be plausibly explained by the vortical flow perturbations associated with the inner mode of K-H surface waves.

3. In comparison with the first interval, during the second interval stronger enhancement was observed in both transverse and compressional components, in both the 1.5–2 and 3.5–4 mHz bands, and over a wider azimuthal range, but the enhancement was much stronger on the duskside than the dawnside. The magnetic field perturbations were not entirely consistent with FLRs, and some characteristics suggested cavity/waveguide resonance. Good correlations are found between the magnetosheath dynamic pressure perturbations, magnetopause deformation, and magnetospheric waves, and all were in good correspondence to IMF discontinuities. We surmise that during the second interval of this event, the perturbations were initially generated at the ion foreshock by these IMF discontinuities. As these foreshock perturbations extended into the magnetosheath and propagated tailward, they likely created transient magnetosheath dynamic pressure perturbations and their forcing on the magnetopause drove the 1.5–2 mHz ULF waves inside the magnetosphere. Concurrently, K-H surface waves continued to drive the 3.5–4 mHz waves.

Acknowledgments

We thank Xiaoyan Xing, Jacob Bortnik, and Wen Li at University of California, Los Angeles, for helpful discussions. The work by C.-P. Wang and R. Thorne has been supported by JHU/APL contracts 967399 and 921647 under NASA's prime contract NAS5-01072. The analysis at UCLA was supported by the EMFISIS subaward 1001057397:01, and the ECT subaward 13-041. The work by M. Hartinger has been supported by NSF AGS-1049403. The work by C. Kletzing was performed under on JHU/APL contract 921647 under NASA Prime contract NAS5-01072. The work by S.G. Claudepierre was supported by RBSP-ECT funding provided by JHU/APL contract 967399 under NASA's prime contract NAS5-01072. All the data used in this study are available for free. Geotail data are provided through the DARTS system by ISAS. We thank T. Mukai at ISAS for the use of the Geotail LEP data. The THEMIS and ARTEMIS data and GOES 13 magnetic field are obtained with the Space Physics Environment Data Analysis System (SPEDAS) software (http://themis.igpp.ucla.edu/software.shtml). We acknowledge NASA contract NAS5-02099 for THEMIS and ARTEMIS, and C.W. Carlson and J.P. McFadden for the use of ESA data and K.H. Glassmeier, U. Auster, and W. Baumjohann for the use of FGM data provided under DLR contract 50-OC-0302. Van Allen Probes (RBSP) electric field data are obtained from http://www.space.umn.edu/rbspefw-data/, magnetic field data from http://emfisis.physics.uiowa.edu/data, and HOPE and MagEIS data from http://www.rbsp-ect.lanl.gov/rbsp_ect.php. We thank J.H. King, N. Papatashvilli at AdnetSystems, NASA GSFC, and CDAWeb for providing the OMNI data. For the ground magnetometer data we gratefully acknowledge SuperMAG PI Jesper W. Gjerloev. We thank the national institutes that support the magnetic observatories and INTERMAGNET (www.intermagnet.org) and SuperMAG (http://supermag.jhuapl.edu/) projects for promoting high standards of magnetic observatory practice. We acknowledge Andre Balogh and Elizabeth Lucek at Imperial College, H. Reme at CESR, and CDAWeb for providing Cluster data.

References

Archer, M. O., T. S. Horbury, J. P. Eastwood, J. M. Weygand, and T. K. Yeoman (2013), Magnetospheric response to magnetosheath pressure pulses: A low-pass filter effect, *J. Geophys. Res. Space Physics*, *118*, 5454–5466, doi:10.1002/jgra.50519.

Archer, M. O., D. L. Turner, J. P. Eastwood, T. S. Horbury, and S. J. Schwartz (2014), The role of pressure gradients in driving sunward magnetosheath flows and magnetopause motion, *J. Geophys. Res. Space Physics*, *119*, 8117–8125, doi:10.1002/2014JA020342.

Archer, M. O., D. L. Turner, J. P. Eastwood, S. J. Schwartz, and T. S. Horbury (2015), Global impacts of a foreshock bubble: Magnetosheath, magnetopause and ground-based observations, *Planet. Space Sci.*, *106*, 56.

Agapitov, O., et al. (2009), Surface waves and field line resonances: A THEMIS case study, *J. Geophys. Res.*, *114*, A00C27, doi:10.1029/2008JA013553.

Auster, H. U., et al. (2008), The THEMIS fluxgate magnetometer, *Space Sci. Rev.*, *141*, 235, doi:10.1007/s11214-008-9365-9.

Balogh, A., et al. (2001), The Cluster magnetic field investigation: Overview of in-flight performance and initial results, *Ann. Geophys.*, *19*, 1207.

Blake, J. B., et al. (2013), The magnetic electron ion spectrometer (MagEIS) instruments aboard the Radiation Belt Storm Probes (RBSP) spacecraft, *Space Sci. Rev.*, *179*, 383–421, doi:10.1007/s11214-013-9991-8.

Bonnell, J. W., F. S. Mozer, G. T. Delory, A. J. Hull, R. E. Ergun, C. M. Cully, V. Angelopoulos, and P. R. Harvey (2008), The Electric Field Instrument (EFI) for THEMIS, *Space Sci. Rev.*, *141*, 303–341.

Chandrasekhar, S. (1961), *Hydrodynamic and Hydromagnetic Stability*, Oxford Univ. Press, Clarendon.

Claudepierre, S. G., S. R. Elkington, and M. Wiltberger (2008), Solar wind driving of magnetospheric ULF waves: Pulsations driven by velocity shear at the magnetopause, *J. Geophys. Res.*, *113*, A05218, doi:10.1029/2007JA012890.

Elkington, S. R., M. K. Hudson, and A. A. Chan (2003), Resonant acceleration and diffusion of outer zone electrons in an asymmetric geomagnetic field, *J. Geophys. Res.*, *108*(A3), 1116, doi:10.1029/2001JA009202.

Erickson, G. M., G. L. Siscoe, D. R. Weimer, K. D. Siebert, M. A. Heinemann, B. U. Ö. Sonnerup, N. C. Maynard, and W. W. White (2002), Prediction of Alfvénic turbulence near the magnetospheric sash, *Planet. Space Sci.*, *2002*(50), 5–6 627.

Eriksson, S., et al. (2016), Magnetospheric multiscale observations of magnetic reconnection associated with Kelvin-Helmholtz waves, *Geophys. Res. Lett.*, *43*, 5606–5615, doi:10.1002/2016GL068783.

Facskó, G., Z. Németh, G. Erdős, A. Kis, and I. Dandouras (2009), A global study of hot flow anomalies using Cluster multi-spacecraft measurements, *Ann. Geophys.*, *27*, 2057–2076, doi:10.5194/angeo-27-2057-2009.

Funsten, H. O., et al. (2013), Helium, Oxygen, Proton, and Electron (HOPE) mass spectrometer for the Radiation Belt Storm Probes mission, *Space Sci. Rev.*, *179*, 423–484, doi:10.1007/s11214-013-9968-7.

Gjerloev, J. W. (2009), A global ground-based magnetometer initiative, *Eos*, *90*, 230–231, doi:10.1029/2009EO270002.

Gjerloev, J. W. (2012), The SuperMAG data processing technique, *J. Geophys. Res.*, *117*, A09213, doi:10.1029/2012JA017683.

Hartinger, M., V. Angelopoulos, M. B. Moldwin, Y. Nishimura, D. L. Turner, K.-H. Glassmeier, M. G. Kivelson, J. Matzka, and C. Stolle (2012), Observations of a Pc5 global (cavity/waveguide) mode outside the plasmasphere by THEMIS, *J. Geophys. Res.*, *117*, A06202, doi:10.1029/2011JA017266.

Hartinger, M. D., D. L. Turner, F. Plaschke, V. Angelopoulos, and H. Singer (2013), The role of transient ion foreshock phenomena in driving Pc5 ULF wave activity, *J. Geophys. Res. Space Physics*, *118*, 299–312, doi:10.1029/2012JA018349.

Hasegawa, A. (1971), Drift wave instabilities of a compressional mode in a high b plasma, *Phys. Rev. Lett.*, *27*, 11–14, doi:10.1103/PhysRevLett.27.11.

Hasegawa, H., et al. (2006), Single-spacecraft detection of rolled-up Kelvin-Helmholtz vortices at the flank magnetopause, *J. Geophys. Res.*, *111*, A09203, doi:10.1029/2006JA011728.

Hietala, H., N. Partamies, T. V. Laitinen, L. B. N. Clausen, G. Facskó, A. Vaivads, H. E. J. Koskinen, I. Dandouras, H. Rème, and E. A. Lucek (2012), Supermagnetosonic subsolar magnetosheath jets and their effects: From the solar wind to the ionospheric convection, *Ann. Geophys.*, *30*, 33–48, doi:10.5194/angeo-30-33-2012.

Hwang, K.-J., M. M. Kuznetsova, F. Sahraoui, M. L. Goldstein, E. Lee, and G. K. Parks (2011), Kelvin-Helmholtz waves under southward interplanetary magnetic field, *J. Geophys. Res.*, *116*, A08210, doi:10.1029/2011JA016596.

Hwang, K.-J. (2015), Magnetopause waves controlling the dynamics of Earth's magnetosphere, *J. Astronomy Space Sci.*, *32*(1), 1–11, doi:10.5140/JASS.2015.32.1.1.

Hwang, K.-J. and D. G. Sibeck (2016), Role of low-frequency boundary waves in the dynamics of the dayside magnetopause and the inner magnetosphere, in *Low-Frequency Waves in Space Plasmas*, edited by A. Keiling, D.-H. Lee, and V. Nakariakov, pp. 213–239, John Wiley, Hoboken, N. J., doi:10.1002/9781119055006.ch13.

Jacobsen, K. S., et al. (2009), THEMIS observations of extreme magnetopause motion caused by a hot flow anomaly, *J. Geophys. Res.*, *114*, A08210, doi:10.1029/2008JA013873.

Karimabadi, H., et al. (2014), The link between shocks, turbulence, and magnetic reconnection in collisionless plasmas, *Phys. Plasmas*, *21*, 062308, doi:10.1063/1.4882875.

Kepko, L., and H. E. Spence (2003), Observations of discrete, global magnetospheric oscillations directly driven by solar wind density variations, *J. Geophys. Res.*, *108*(A6), 1257, doi:10.1029/2002JA009676.

King, J. H., and N. E. Papitashvili (2005), Solar wind spatial scales in and comparisons of hourly Wind and ACE plasma and magnetic field data, *J. Geophys. Res.*, *110*, A02104, doi:10.1029/2004JA010649.

Kivelson, M. G., and D. J. Southwood (1986), Coupling of global magnetospheric MHD eigenmodes to field line resonances, *J. Geophys. Res.*, *91*(A4), 4345–4351, doi:10.1029/JA091iA04p04345.

Kletzing, C. A., et al. (2013), The Electric and Magnetic Field Instrument Suite and Integrated Science (EMFISIS) on RBSP, *Space Sci. Rev.*, *179*, 127–181, doi:10.1007/s11214-013-9993-6.

Kokubun, S., T. Yamamoto, M. H. Acuna, K. Hayashi, K. Shiokawa, and H. Kawano (1994), The Geotail magnetic field experiment, *J. Geomag. Geoelec.*, *46*, 7–21.

Korotova, G. I., and D. G. Sibeck (1995), A case study of transient event motion in the magnetosphere and in the ionosphere, *J. Geophys. Res.*, *100*, 35.

Lee, L. C., R. K. Albano, and J. R. Kan (1981), Kelvin-Helmholtz instability in the magnetopause-boundary layer region, *J. Geophys. Res.*, *86*, 54–58.

Li, W. Y., X. C. Guo, and C. Wang (2012), Spatial distribution of Kelvin-Helmholtz instability at low-latitude boundary layer under different solar wind speed conditions, *J. Geophys. Res.*, *117*, A08230, doi:10.1029/2012JA017780.

Li, W., C. Wang, B. Tang, X. Guo, and D. Lin (2013), Global features of Kelvin-Helmholtz waves at the magnetopause for northward interplanetary magnetic field, *J. Geophys. Res. Space Physics*, *118*, 5118–5126, doi:10.1002/jgra.50498.

Liu, Z., D. L. Turner, V. Angelopoulos, and N. Omidi (2015), THEMIS observations of tangential discontinuity-driven foreshock bubbles, *Geophys. Res. Lett.*, *42*, 7860–7866, doi:10.1002/2015GL065842.

Lucek, E. A., T. S. Horbury, A. Balogh, I. Dandouras, and H. Rème (2004), Cluster observations of hot flow anomalies, *J. Geophys. Res.*, *109*, A06207, doi:10.1029/2003JA010016.

McFadden, J. P., C. W. Carlson, D. Larson, V. Angelopoulos, M. Ludlam, R. Abiad, B. Elliott, P. Turin, and M. Marckwordt (2008), The THEMIS ESA plasma instrument and in-flight calibration, *Space Sci. Rev*, *141*, 277, doi:10.1007/s11214-008-9440-2.

McGregor, S. L., M. K. Hudson, and W. J. Hughes (2014), Modeling magnetospheric response to synthetic Alfvénic fluctuations in the solar wind: ULF wave fields in the magnetosphere, *J. Geophys. Res. Space Physics*, *119*, 8801–8812, doi:10.1002/2014JA020000.

McPherron, R. L. (2005), Magnetic pulsations: Their sources and relation to solar wind and geomagnetic activity, *Surv. Geophys.*, *26*, 545, doi:10.1007/s10712-005-1758-7.

Merkin, V. G., J. G. Lyon, and S. G. Claudepierre (2013), Kelvin-Helmholtz instability of the magnetospheric boundary in a three-dimensional global MHD simulation during northward IMF conditions, *J. Geophys. Res. Space Physics*, *118*, 5478–5496, doi:10.1002/jgra.50520.

Mukai, T., S. Machida, Y. Saito, M. Hirahara, T. Terasawa, N. Kaya, T. Obara, M. Ejiri, and A. Nishida (1994), The low-energy particle (LEP) experiment onboard the Geotail satellite, *J. Geomag. Geoelec.*, *46*, 669–692.

Nakamura, T. K. M., M. Fujimoto, and A. Otto (2006), Magnetic reconnection induced by weak Kelvin-Helmholtz instability and the formation of the low-latitude boundary layer, *Geophys. Res. Lett.*, *33*, L14106, doi:10.1029/2006GL026318.

Němeček, Z., J. Šafránková, L. Prech, D. G. Sibeck, S. Kokubun, and T. Mukai (1998), Transient flux enhancements in the magnetosheath, *Geophys. Res. Lett.*, *25*, 1273–1276, doi:10.1029/98GL50873.

Nishida, A. (1978), *Geomagnetic Diagnosis of the Magnetosphere*, Springer, Berlin.

Nowada, M., J.-H. Shue, C.-H. Lin, T. Sakurai, D. G. Sibeck, V. Angelopoulos, C. W. Carlson, and H.-U. Auster (2009), Alfvénic plasma velocity variations observed at the inner edge of the low-latitude boundary layer induced by the magnetosheath mirror mode waves: A THEMIS observation, *J. Geophys. Res.*, *114*, A07208, doi:10.1029/2008JA014033.

O'Brien, T. P., R. L. McPherron, D. Sornette, G. D. Reeves, R. Friedel, and H. J. Singer (2001), Which magnetic storms produce relativistic electrons at geosynchronous orbit?, *J. Geophys. Res.*, *106*(A8), 15533–15544, doi:10.1029/2001JA000052.

Omidi, N., and D. Sibeck (2007), Formation of hot flow anomalies and solitary shocks, *J. Geophys. Res.*, *112*, A01203, doi:10.1029/2006JA011663.

Omidi, N., J. P. Eastwood, and D. G. Sibeck (2010), Foreshock bubbles and their global magnetospheric impacts, *J. Geophys. Res.*, *115*, A06204, doi:10.1029/2009JA014828.

Omidi, N., D. Sibeck, O. Gutynska, and K. J. Trattner (2014), Magnetosheath filamentary structures formed by ion acceleration at the quasi-parallel bow shock, *J. Geophys. Res. Space Physics*, *119*, 2593–2604, doi:10.1002/2013JA019587.

Omidi, N., J. Berchem, D. Sibeck, and H. Zhang (2016), Impacts of spontaneous hot flow anomalies on the magnetosheath and magnetopause, *J. Geophys. Res. Space Physics*, *121*, 3155–3169, doi:10.1002/2015JA022170.

Peredo, M., J. A. Slavin, E. Mazur, and S. A. Curtis (1995), Three-dimensional position and shape of the bow shock and their variation with Alfvénic, sonic and magnetosonic Mach numbers and interplanetary magnetic field orientation, *J. Geophys. Res.*, *100*(A5), 7907–7916, doi:10.1029/94JA02545.

Plaschke, F., M. G. G. T. Taylor, and R. Nakamura (2014), Alternative interpretation of results from Kelvin-Helmholtz vortex identification criteria, *Geophys. Res. Lett.*, *41*, 244–250, doi:10.1002/2013GL058948.

Rae, I. J., et al. (2005), Evolution and characteristics of global Pc5 ULF waves during a high solar wind speed interval, *J. Geophys. Res.*, *110*, A12211, doi:10.1029/2005JA011007.

Reeves, G. D., K. L. McAdams, R. H. W. Friedel, and T. P. O'Brien (2003), Acceleration and loss of relativistic electrons during geomagnetic storms, *Geophys. Res. Lett.*, *30*, 1529, doi:10.1029/2002GL016513.

Rème, H., et al. (2001), First multispacecraft ion measurements in and near the Earth's magnetosphere with the identical Cluster ion spectrometry (CIS) experiment, *Ann. Geophys.*, *19*, 1303–1354.

Rickard, G. J., and A. N. Wright (1995), ULF pulsations in a magnetospheric waveguide: Comparison of real and simulated satellite data, *J. Geophys. Res.*, *100*(A3), 3531–3537.
Roelof, E. C., and D. G. Sibeck (1993), Magnetopause shape as a bivariate function of interplanetary magnetic field B_z and solar wind dynamic pressure, *J. Geophys. Res.*, *98*(A12), 21,421–21,450, doi:10.1029/93JA02362.
Rostoker, G., S. Skone, and D. N. Baker (1998), On the origin of relativistic electrons in the magnetosphere associated with some geomagnetic storms, *Geophys. Res. Lett.*, *25*(19), 3701–3704, doi:10.1029/98GL02801.
Samson, J. C., B. G. Harrold, J. M. Ruohoniemi, R. A. Greenwald, and A. D. M. Walker (1992), Field line resonances associated with MHD waveguides in the magnetosphere, *Geophys. Res. Lett.*, *19*(5), 441–444, doi:10.1029/92GL00116.
Schwartz, S. J., et al. (1985), An active current sheet in the solar wind, *Nature*, *318*, 269–271, doi:10.1038/318269a0.
Schwartz, S. J. (1998), Shock and discontinuity normal, Mach numbers, and related parameters, in *Analysis Methods for Multi-Spacecraft Data, ISSI Sci. Rep. SR-001*, edited by G. Paschmann and P. W. Daly, pp. 249–270, ISSI/ESA, Noordwijk, Netherlands.
Seough, J., and P. H. Yoon (2012), Quasilinear theory of anisotropy-beta relations for proton cyclotron and parallel firehose instabilities, *J. Geophys. Res.*, *117*, A08101, doi:10.1029/2012JA017645.
Sibeck, D. G., R. P. Lepping, and A. J. Lazarus (1990), Magnetic field line draping in the plasma depletion layer, *J. Geophys. Res.*, *95*, 2433–2440, doi:10.1029/JA095iA03p02433.
Sibeck, D. G., et al. (1999), Comprehensive study of the magnetospheric response to a hot flow anomaly, *J. Geophys. Res.*, *104*(A3), 4577–4593, doi:10.1029/1998JA900021.
Siscoe, G. L. (1983), Solar system magnetohydrodynamics, in *Solar-Terrestrial Physics*, edited by R. L. Carovillano and J. M. Forbes, pp. 11–100, D. Reidel, Norwell, Mass.
Singer, H., L. Matheson, R. Grubb, A. Newman, and D. Bouwer (1996), Monitoring space weather with the GOES magnetometers, in *GOES-8 and Beyond*, vol. 2812, edited by E. R. Washwell, pp. 299–308, Soc. of Photo-Optical Instrum. Eng, Bellingham, Wash.
Smith, C. W., J. L'Heureux, N. F. Ness, M. H. Acuna, L. F. Burlaga, and J. Scheifele (1998), The ACE magnetic fields experiment, *Space Sci. Rev.*, *86*, 613.
Sonnerup, B. U. O., and M. Scheible (1998), Minimum and maximum variance analysis, in *Analysis Methods for Multi-Spacecraft Data*, *ISSI Sci. Rep. SR-001*, edited by G. Paschmann and P. W. Daly, pp. 185–220, Eur. Space Agency Publ. Dif, Noordwijk, Netherlands.
Southwood, D. J., and M. G. Kivelson (1991), An approximate description of field-aligned currents in a planetary magnetic field, *J. Geophys. Res.*, *96*(A1), 67–75, doi:10.1029/90JA01806.
Spence, H. E., et al. (2013), Science goals and overview of the Radiation Belt Storm Probes (RBSP) Energetic Particle, Composition, and Thermal Plasma (ECT) suite on NASA's Van Allen Probes mission, *Space Sci. Rev.*, *179*, 311–336, doi:10.1007/s11214-013-0007-5.
Takagi, K., C. Hashimoto, H. Hasegawa, M. Fujimoto, and R. TanDokoro (2006), Kelvin-Helmholtz instability in a magnetotail flank-like geometry: Three-dimensional MHD simulations, *J. Geophys. Res.*, *111*, A08202, doi:10.1029/2006JA011631.
Takahashi, K., D. G. Sibeck, P. T. Newell, and H. E. Spence (1991), ULF waves in the low-latitude boundary layer and their relationship to magnetospheric pulsations: A multisatellite observation, *J. Geophys. Res.*, *96*(A6), 9503–9519, doi:10.1029/91JA00612.
Taylor, M. G. G. T., et al. (2012), Spatial distribution of rolled-up Kelvin-Helmholtz vortices at Earth's dayside and flank magnetopause, *Ann. Geophys.*, *30*, 1025–1035, doi:10.5194/angeo-30-1025-2012.
Tamao, T. (1965), Transmission and coupling resonance of hydromagnetic disturbances in the nonuniform Earth's magnetosphere, *Sci. Rep. Tohoku Univ. Geophys.*, *17*, 43–72.
Thomsen, M. F., J. T. Gosling, S. A. Fuselier, S. J. Bame, and C. T. Russell (1986), Hot, diamagnetic cavities upstream from the Earth's bow shock, *J. Geophys. Res.*, *91*(A3), 2961–2973, doi:10.1029/JA091iA03p02961.
Tsyganenko, N. A. (2002a), A model of the near magnetosphere with a dawn-dusk asymmetry: 1. Mathematical structure, *J. Geophys. Res.*, *107*, 1179, doi:10.1029/2001JA000219.
Tsyganenko, N. A. (2002b), A model of the near magnetosphere with a dawn-dusk asymmetry: 2. Parameterization and fitting to observations, *J. Geophys. Res.*, *107*, 1176, doi:10.1029/2001JA000220.
Turner, D. L., N. Omidi, D. G. Sibeck, and V. Angelopoulos (2013), First observations of foreshock bubbles upstream of Earth's bow shock: Characteristics and comparisons to HFAs, *J. Geophys. Res. Space Physics*, *118*, 1552–1570, doi:10.1002/jgra.50198.
Viall, N. M., L. Kepko, and H. E. Spence (2009), Relative occurrence rates and connection of discrete frequency oscillations in the solar wind density and dayside magnetosphere, *J. Geophys. Res.*, *114*, A01201, doi:10.1029/2008JA013334.
Wygant, J. R., et al. (2013), The electric field and waves instruments on the Radiation Belt Storm Probes mission, *Space Sci. Rev.*, *179*, 183–220, doi:10.1007/s11214-013-0013-7.
Zhang, H., D. G. Sibeck, Q.-G. Zong, S. P. Gary, J. P. McFadden, D. Larson, K.-H. Glassmeier, and V. Angelopoulos (2010), Time History of Events and Macroscale Interactions during Substorms observations of a series of hot flow anomaly events, *J. Geophys. Res.*, *115*, A12235, doi:10.1029/2009JA015180.
Zhang, H., D. Sibeck, Q. G. Zong, N. Omidi, D. Turner, and L. N. Clausen (2013), Spontaneous hot flow anomalies at quasi-parallel shocks: 1. Observations, *J. Geophys. Res. Space Physics*, *118*, 1–7, doi:10.1002/jgra.50376.